

Silicon Modulators and Germanium Photodetectors on SOI: Monolithic Integration, Compatibility, and Performance Optimization

Tsung-Yang Liow, *Member, IEEE*, Kah-Wee Ang, *Member, IEEE*, Qing Fang, Jun-Feng Song, Yong-Zhong Xiong, *Senior Member, IEEE*, Ming-Bin Yu, Guo-Qiang Lo, *Member, IEEE*, and Dim-Lee Kwong, *Fellow, IEEE*

Abstract—Si modulators and Ge photodetectors are monolithically integrated on Si-on-insulator. The carrier-depletion-type Si modulators achieved high modulation efficiency and speed ($V_{\pi}L_{\pi} = 2.56 \text{ V}\cdot\text{cm}$, 10 Gb/s). Low-voltage operation ($V_{\text{RF}} = 1 V_{\text{pp}}$) was also demonstrated. Introducing a low-thermal-budget postepitaxy anneal improves the performance of the Ge photodetectors, thus resulting in significantly improved dark current. The responsivity and speed in the low-voltage regime are also enhanced, which enhances low-voltage or even short-circuit ($V_{\text{Bias}} = 0 \text{ V}$) operation.

Index Terms—Germanium photodetector, monolithic integration, silicon modulator, silicon photonics.

I. INTRODUCTION

WITH the introduction of new and even personalized high-bandwidth content services, the surge in demand for high-speed consumer connectivity reveals bottlenecks in existing network infrastructure. Cost-effective interface solutions, which are capable of data rates of 10 Gb/s and beyond, are sought. In addition, multiple channel transmission over a single fiber is desirable for the scalability of the aggregate data rates. By tapping on the volume manufacturing capability of the Si CMOS platform, Si photonics can potentially offer cost-effective yet high-performance optical interface solutions, and will be especially important in short-reach applications.

Numerous challenges lie ahead for monolithically integrated Si photonics [1]. There are process integration and thermal budget constraints when monolithically integrating Si photonic

Manuscript received May 1, 2009; revised May 27, 2009. First published November 10, 2009; current version published February 5, 2010.

T.-Y. Liow, K.-W. Ang, Q. Fang, Y.-Z. Xiong, M.-B. Yu, and G.-Q. Lo are with the Institute of Microelectronics, Agency for Science, Technology and Research (A*STAR), Singapore 117685, Singapore (e-mail: liowty@ime.a-star.edu.sg; angkw@ime.a-star.edu.sg; fangq@ime.a-star.edu.sg; yongzhong@ime.a-star.edu.sg; mingbin@ime.a-star.edu.sg; logq@ime.a-star.edu.sg).

J.-F. Song is with the Institute of Microelectronics, Agency for Science, Technology and Research (A*STAR), Singapore 117685, Singapore, and also with the State Key Laboratory on Integrated Opto-Electronics, College of Electronic Science and Engineering, Jilin University, Changchun 130023, China (e-mail: songjf@ime.a-star.edu.sg).

D.-L. Kwong is with the Institute of Microelectronics, Agency for Science, Technology and Research (A*STAR), Singapore 117685, Singapore, and also with the National University of Singapore, Singapore 119077, Singapore. He is also with Republic Polytechnic, Singapore 738964, Singapore (e-mail: kwongdl@ime.a-star.edu.sg).

Color versions of one or more of the figures in this paper are available online at <http://ieeexplore.ieee.org>.

Digital Object Identifier 10.1109/JSTQE.2009.2028657

components and CMOS on the same chip. Pinguet *et al.* have reported a demonstration of such an approach [2], but did not elaborate on the details. Modulators and photodetectors are two key active components in an optical transceiver. In this paper, the CMOS-compatible monolithic integration of the Si modulator and the Ge photodetector, together with details of how the performance can be optimized, is discussed. Besides process compatibility, the modulators and photodetectors should possess high efficiency and the ability to operate at low power supply voltages. The methods to achieve this are also discussed.

There have been several reports on Si modulators based on the free-carrier plasma dispersion effect [3]–[15]. The Mach-Zehnder Si waveguide modulator based on a p-n junction phase shifter operated in reverse bias (carrier depletion) shows great potential for wideband high-speed performance and is the focus of this paper. Depletion mode operation allows the speed to be insensitive to the carrier lifetime, as shown by simulations in [4]. Experimentally, modulation speeds of up to 40 Gb/s have been demonstrated, albeit with a low extinction ratio (ER) of 1.1 dB [15]. For 10 Gb/s operation, they reported an ER of 5.2 dB for a modulator with 3-mm-long phase shifters, which were driven differentially with RF signals of $7.6 V_{\text{pp}}$ each. In this paper, we fabricated a carrier-depletion-type modulator with comparable if not better $V_{\pi}L_{\pi}$ compared with the best reported carrier-depletion-type modulators [2]–[7]. For 10 Gb/s operation, an ER of 6.1 dB was achieved for a modulator with a 2-mm-long phase shifter, which was driven single-endedly with an RF signal of $5 V_{\text{pp}}$.

Due to its inherently large bandgap, Si itself cannot be used efficiently for photodetection at wavelengths commonly used for optical fiber communications (1.3–1.55 μm). This can be addressed by introducing a material with a smaller bandgap, such as Ge, SiGe [16]–[18] and Ge photodetectors [19]–[33] have been successfully integrated on Si previously. Waveguided Ge photodetectors are particularly attractive due to their high responsivity at 1.55 μm . This is because the regions of absorption can be made much longer to enable full absorption, despite the long absorption length of 1.55 μm wavelengths in Ge. There have also been reports on photodetector approaches using polycrystalline Ge [31], [32], which is appealing due to its low cost and thermal budget. However, due to the poor crystalline quality, the carrier diffusion length is short, thus imposing constraints on the photodetector design, which results in inferior responsivity and speed compared to photodetectors using epitaxial

monocrystalline Ge. Another low-thermal-budget approach involves a wafer bonding and ion-cut process for integrating the Ge photodetector [33]. Although the approach shows great potential, the process is also more complex. In this paper, selective heteroepitaxy of Ge is used in the monolithic integration of Ge photodetectors.

II. MONOLITHIC INTEGRATION OF Si MODULATORS AND Ge PHOTODETECTORS

Si waveguide modulators based on carrier depletion and waveguided Ge photodetectors are monolithically integrated on Si-on-insulator (SOI) wafers using a process integration flow that is compatible with CMOS integration, both in terms of thermal budget and fabrication feasibility. The simplified process flow is shown in Fig. 1. SOI wafers with a top Si thickness of 220 nm and buried oxide thickness of 2 μm were used. The rib and channel waveguides were formed by anisotropic dry etching, after which the p^{++} , p , n , n^{++} implants for the Si modulator were performed. For the anode formation of the Ge vertical n - i - p photodetectors (VPDs), p -type implants were performed with two dose splits (“ p^+ -Si” and “ p -Si”). For comparison purposes, lateral photodetectors (LPDs) were also fabricated on similarly doped substrates, in addition to being fabricated on an undoped substrate. The implanted dopants in Si were activated using a rapid thermal anneal (RTA) at 1030 $^{\circ}\text{C}$ for 5 s prior to Ge epitaxy. After depositing a 60-nm-thick SiO_2 layer, windows were etched in SiO_2 using an anisotropic dry etch followed by a wet etch, so as to ensure that the Si surface is not damaged by the reactive ion etching process. Ge was then selectively grown to a thickness of 500 nm in an ultrahigh vacuum chemical vapor deposition (UHVCVD) epitaxy reactor at 550 $^{\circ}\text{C}$. Details of the epitaxy process are similar to that reported in [30], except that the Ge thickness in this case is 500 nm. The top view optical micrograph and SEM images of a Si modulator and a Ge photodetector after the Ge epitaxy step are shown in Fig. 2. Some splits further underwent a postepitaxy annealing step at 750 $^{\circ}\text{C}$ for 30 min, which improves the performance of the photodetector. The effects of this anneal will be discussed in later sections. Ion implantation was then performed for the Ge regions. These dopants in Ge were activated by annealing at 500 $^{\circ}\text{C}$ for 5 min. The fabrication process was completed after the formation of contact vias and aluminum interconnects.

III. MONOLITHICALLY INTEGRATED Si MODULATORS

The Si modulator utilizes the free-carrier dispersion effect and is based on a Mach–Zehnder interferometer (MZI) design, as shown in Fig. 3(a). A lateral p - n junction is fabricated in each phase-shifter arm. For high-speed performance, the p - n junction phase shifters are operated in the depletion mode [2]–[7]. The free carrier density in the rib waveguide is modulated by varying the depletion width of the p - n junction. The change in refractive index is related to the change in carrier concentration [34] and can be described by the Drude–Lorenz equations. It is of particular importance to note that free holes are more effective in perturbing the index than free electrons.

- Waveguide (Channel and Rib) pattern and etch
- Si modulator p^{++} , p , n , n^{++} implants
- Ge vertical n - i - p photodetector anode implants:
“ p^+ -Si sub”: $5 \times 10^{14} \text{ cm}^{-2}$ Boron
“ p -Si sub”: $1 \times 10^{14} \text{ cm}^{-2}$ Boron
- Implant activation for dopants in Si (RTA 1030 $^{\circ}\text{C}$, 5s)
- Ge epitaxy window patterning
- Ge selective epitaxial growth (500 nm, 550 $^{\circ}\text{C}$)
- Ge anneal for performance enhancement, 750 $^{\circ}\text{C}$, 30min
- Ge photodetector implantation
“LPD”: p^+ , n^+ implants
“VPD”: n^+ implant
- Implant activation for dopants in Ge (500 $^{\circ}\text{C}$, 5 min)
- Formation of contact vias and Al interconnects

Fig. 1. Simplified process flow showing the key steps for fabricating the monolithically integrated Si modulators and Ge photodetectors.

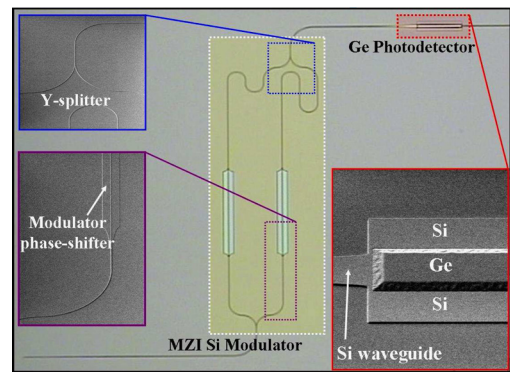


Fig. 2. Optical micrograph showing a monolithically integrated Si modulator and Ge photodetector after Ge epitaxy. SEM images (inset) show a modulator's phase shifter (rib waveguide) and Y-splitter (channel waveguide), as well as a Ge photodetector structure.

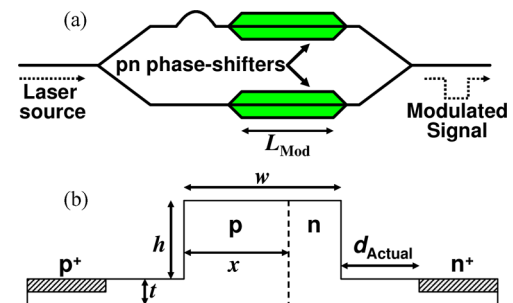


Fig. 3. (a) Si modulator test structure schematic showing the MZI-based design. (b) Cross-sectional schematic showing the p - n junction phase shifter and key structural parameters (h , w , t , x , t , and d_{Actual}).

The cross-sectional schematic of the p - n junction phase shifter is shown in Fig. 3(b). The key structural parameters are the rib height (h), rib width (w), slab thickness (t), p - n junction location (x), and the rib-to-contact distance (d_{Actual}). In these experiments, the value of w is 600 nm. For high phase-shifting efficiency, it is desirable to have maximum interaction between the optical mode and the regions of hole density change. This can be achieved by tightly confining the optical mode within the rib waveguide, as well as by controlling the dopant profile and the location of the p - n junction.

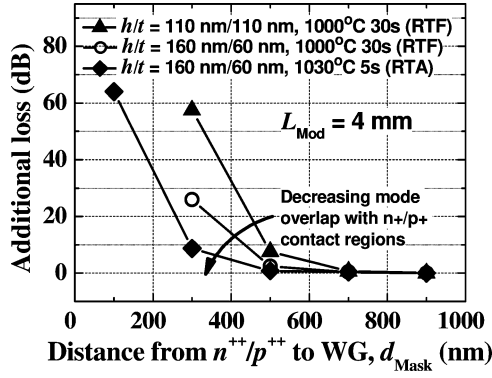


Fig. 4. Higher ratio of h to t results in better lateral mode confinement, and hence, reduced additional optical loss as d_{Mask} is reduced. Using an RTA spike anneal (1030 °C, 5 s) for implant activation also reduces lateral dopant diffusion compared to RTF anneal (1000 °C, 30 s).

Due to the high index contrast in the SOI platform, submicrometer waveguides with tight optical mode confinement can be realized. For a rib waveguide, the optical mode becomes more laterally confined as the ratio of h/t increases. This was experimentally confirmed by loss measurements on modulator test structures with different lithographic distances between the rib and the highly doped contact regions d_{Mask} . Any modal overlap with the highly doped n^{++}/p^{++} contact regions will result in additional optical loss. This additional optical loss was experimentally extracted and plotted for different values of d_{Mask} in Fig. 4. At values of d_{Mask} that are 700 nm and above, there is negligible additional optical loss due to optical absorption by the contact regions for all splits. This indicates that the optical mode does not extend to the regions that are laterally at least 700 nm away from the rib for all splits. The difference between the splits is obvious at values of d_{Mask} , which are at or below 500 nm. An h/t ratio of 160 nm/60 nm results in better lateral mode confinement than 110 nm/110 nm, which, in turn, results in reduced additional loss. RTA implant activation is known to result in less dopant diffusion than furnace-type activation in a rapid thermal furnace (RTF), and will hence result in a larger actual distance between the rib and the highly doped contact regions d_{Actual} for a given d_{Mask} . Fig. 4 also shows that when RTA activation is used instead of RTF activation, the additional loss is reduced for a given value of d_{Mask} below 500 nm. This further confirms the cause of the additional loss to be due to dopant absorption in the contact regions. It is apparent that the structural design of the modulator has a large impact on the loss and the degree of mode confinement. Hence, such experimental test structures are of significant aid to the optimization process.

The implant conditions were chosen such that the concentration of p-type dopants exceeds that of n-type dopants, so that the location of the p-n junction is determined primarily by the p-type dopant implant. For the n and p implants in the rib, dopants were implanted at two energy levels to control the vertical distribution. The doping concentration in the waveguide rib can be obtained with the help of TCAD process simulations, as shown in Fig. 5.

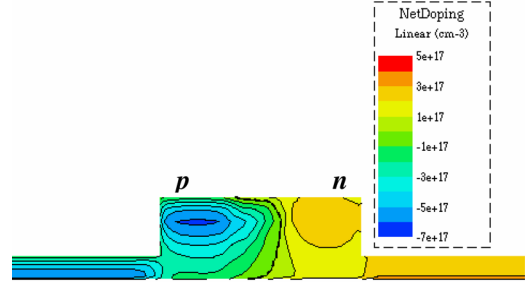


Fig. 5. Simulated net doping concentration in the rib waveguide. Two ion implantation energy values were used for each p and n implants, respectively.

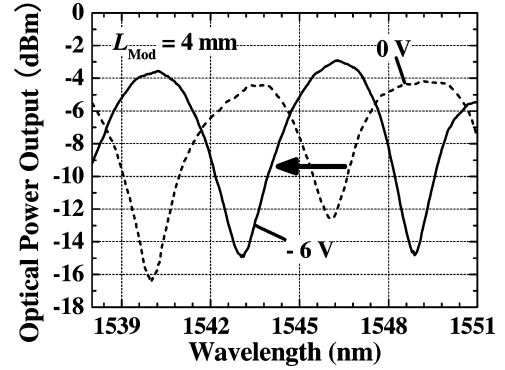


Fig. 6. Output spectra of a modulator with a 4-mm-long phase shifter at applied phase-shifter voltages of 0 and -6 V.

The output spectra of a modulator with a 4-mm-long phase shifter for bias voltages of 0 and -6 V are shown in Fig. 6. The relative phase shift $\Delta\varphi$ can be extracted from Fig. 6 using

$$\Delta\varphi = \frac{2\pi\Delta\lambda}{\text{FSR}}. \quad (1)$$

The free spectral range (FSR) of the asymmetric MZI is ~ 6 nm. At -6.4 V, $\Delta\lambda$ is ~ 3 nm, giving a $V_{\pi}L_{\pi}$ of 2.56 V·cm, where V_{π} and L_{π} are the applied phase-shifter voltage and length required to obtain a $\Delta\varphi$ of π . The phase-shifting efficiency is comparable to or exceeds those of reported carrier-depletion-type modulators [2]–[7]. The normalized loss caused by the phase shifters (both arms) was extracted to be ~ 1 dB/mm. For minimum loss and device footprint, the modulator phase shifters should be as short as possible. For a given driving voltage, a low $V_{\pi}L_{\pi}$ value can allow suitable reduction of the phase-shifter length.

Fig. 7 plots $\Delta\varphi$ and normalized capacitance at different phase-shifter voltages. Phase shifting is more efficient in the voltage regime between -1 and $+0.7$ V. This is expected since the carrier concentration depends on the depletion width, which is proportional to the square root of the total electrostatic potential difference across the junction (taking the simple example of uniform doping). Qualitatively, this means that larger changes in depletion width occur when the total electrostatic potential difference is small. On the other hand, the improvement in phase-shifting efficiency in the high-efficiency regime comes at the expense of speed, since the normalized capacitance

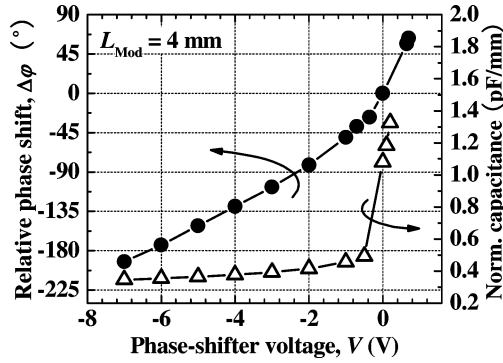


Fig. 7. Relative phase shift and normalized capacitance at different phase-shifter voltages. The phase-shifting efficiency is higher for phase-shifter voltages from -1 to $+0.7$ V. However, the normalized capacitance is also higher due to the smaller depletion width of the p-n junction.

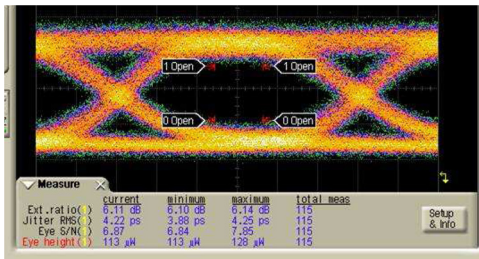


Fig. 8. High-speed operation: modulator with 2-mm-long phase shifter driven at 10 Gb/s in single-ended mode ($V_{dc} = -3.75$ V, $V_{RF} = 5 V_{pp}$). ER is 6.1 dB.

at lower reverse bias voltages is also higher due to the smaller depletion width. Depending on the requirements, the operating point of the modulator can be chosen by varying the dc bias. Two examples are shown here to qualitatively illustrate this.

High-speed operation was tested by driving a modulator with a 2-mm-long phase shifter in single-ended mode (only one arm is driven). The dc-coupled signal to the phase-shifter input comprised a dc bias voltage (V_{dc}) of -3.75 V combined with an RF signal (V_{RF}) of $5 V_{pp}$ using a bias tee. The chosen dc bias voltage ensures that the phase shifter is operated in the low-capacitance regime. The RF signal was from a pseudorandom bit sequence (PRBS) source with a pattern length of $[2^7 - 1]$ bits. The phase-shifter output was externally terminated with a 50Ω resistor. An ER of ~ 6.1 dB was measured at 10 Gb/s (Fig. 8), which is the limit of the measurement equipment used. The short rise/fall times indicate that even higher speed is possible. The measured jitter was ~ 4.2 ps.

Low-voltage operation was then tested by driving the modulator differentially (both arms driven simultaneously). In addition, the dc bias voltage can also be chosen such that the phase shifter operates in the regime of higher phase efficiency (-1 to $+0.7$ V). A modulator with 4-mm-long phase shifters was driven differentially using a low-voltage 3.125 Gb/s PRBS signal source ($V_{dc} = 0$ V, $V_{RF} = 1 V_{pp}$). The measured ER and jitter are ~ 5.1 dB and ~ 13.5 ps, respectively (Fig. 9). The measured ER is degraded by the shape of the eye pattern due to the lower device speed. The measured ER at 1.25 Gb/s is ~ 6.1 dB. The low RF driving voltage will potentially allow the modulator to

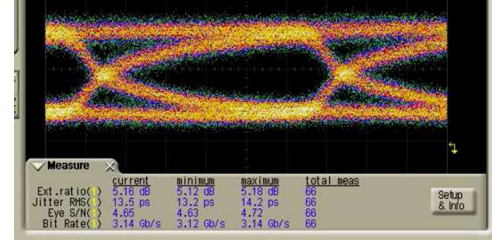


Fig. 9. Low-voltage operation: modulator with 4-mm-long phase shifters driven at 3.125 Gb/s in differential mode ($V_{dc} = 0$ V, $V_{RF} = 1 V_{pp}$). ER is 5.1 dB.

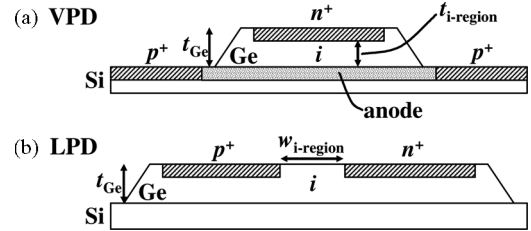


Fig. 10. Cross-sectional schematics of the VPD and the LPD. The length of the Ge regions for all photodetectors in this paper is $100 \mu\text{m}$. Width of the Ge region is $8 \mu\text{m}$ for VPDs and $19 \mu\text{m}$ for LPDs.

be driven by monolithically integrated CMOS driving circuits. The modulation speed can be improved by reducing the parasitic series resistance (extracted to be 8.2Ω), which can be achieved by increasing the slab doping concentration and by contact silicidation.

IV. MONOLITHICALLY INTEGRATED WAVEGUIDED Ge PHOTODETECTORS

Two types of Ge photodetector structures were fabricated. Fig. 10 shows the cross-sectional schematics of the VPD and LPD. The VPD has a vertical n-i-p junction whereas the LPD has a lateral p-i-n junction. The thickness of the intrinsic region ($t_{i\text{-region}}$) in the VPD is determined by the thickness of Ge grown (t_{Ge}) and the thickness of the n^+ region, which can be controlled by the epitaxy conditions and the doping conditions, respectively. The width of the intrinsic region ($w_{i\text{-region}}$) in the LPD can be controlled by the lithographically defined spacing between the p^+ and n^+ contacts. The speed of the photodetectors can be maximized by optimizing $t_{i\text{-region}}$ and $w_{i\text{-region}}$, respectively [25], [26]. The length can also be reduced from $100 \mu\text{m}$ that was used for these test devices. Nevertheless, improving the absolute speed is not the focus of this paper. Instead, this paper focuses on the performance optimization of the Ge photodetectors, particularly for low-voltage operation. A new figure of merit is also proposed to aid in the analysis and optimization of photodetectors for low-voltage operation.

Previously, it has been reported that postepitaxy annealing involving high thermal budget (up to 900°C furnace-type annealing) can improve Ge film quality [22]–[24]. Here, we show that by inserting a low-thermal-budget anneal step after Ge epitaxial growth, the photodetector dark current (I_{Dark}) is already significantly reduced. At the same time, the responsivity and speed in the low-voltage regime are also improved. Fig. 11 shows

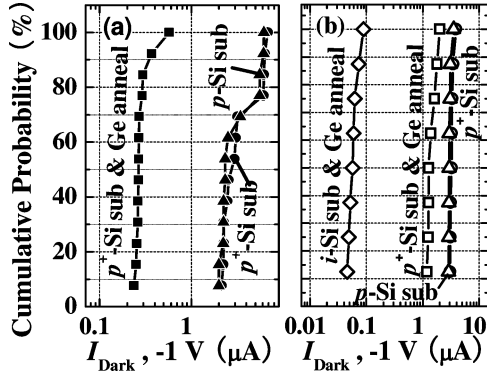


Fig. 11. Dark current statistics of (a) VPDs and (b) LPDs. The results clearly show the improvement in I_{Dark} in both VPD and LPD after the Ge anneal. For LPDs, using an undoped Si substrate improves I_{Dark} by more than one order of magnitude.

the I_{Dark} statistics of (a) VPDs and (b) LPDs. For both VPDs and LPDs, using p^+ -Si (implant dose = $5 \times 10^{-14} \text{ cm}^{-2}$) or p -Si (implant dose = $1 \times 10^{-14} \text{ cm}^{-2}$) substrates has negligible impact on I_{Dark} . This indicates that p^+ -Si anodes are preferable for fabricating VPDs with lower parasitic resistances. The postepitaxy anneal process at 750°C for 30 min improves I_{Dark} for VPDs by about one order of magnitude to $\sim 260 \text{ nA}$. Conversely, I_{Dark} for LPDs is only reduced by about 60%. This can perhaps be explained by the enhanced upward diffusion of boron from the p^+ -Si substrate into the intrinsic Ge regions for the VPD. The high density of defects at the Ge-Si interface is electrically “deactivated” since they are now located in the p^+ region. Another possible reason is the more effective annihilation of defects nearer the Ge-Si interface, which affects VPDs more than LPDs. For LPDs, the substrate below the Ge film need not be doped. For the LPD split fabricated on an undoped Si substrate, I_{Dark} ($\sim 60 \text{ nA}$) was more than one order of magnitude less than those fabricated on the p -doped substrates. Fig. 12 shows the extracted activation energy (E_a) at different reverse bias voltages for (a) VPDs and (b) LPDs, respectively, using temperature measurements [35], [36]. For the PDs without anneal, the E_a values are close to half the Ge bandgap, which suggests that the transport process is likely to be dominated by the trap-assisted generation in the depletion region (Shockley-Read-Hall process). For the PDs that have been subjected to the Ge anneal, there is a substantial increase in E_a , suggesting a shift in the transport mechanism toward one of band-to-band generation due to the reduction in defect density.

I_{Dark} is important as it is related to the dark shot noise I_n by

$$I_n = \sqrt{2qI_{\text{Dark}}B} \quad (2)$$

(where q is the electron charge and B is the bandwidth) [37], and hence affects the SNR. As can be observed from Fig. 13, temperature has a huge impact on I_{Dark} . It is clear that I_{Dark} depends not only on bias voltage, but is significantly affected by the temperature as well. As such, evaluation of I_{Dark} should be performed using a contour plot. Fig. 14 shows the contour plot of I_{Dark} for different temperature and bias voltage conditions for the best performing VPD split (p^+ -Si sub and anneal). The

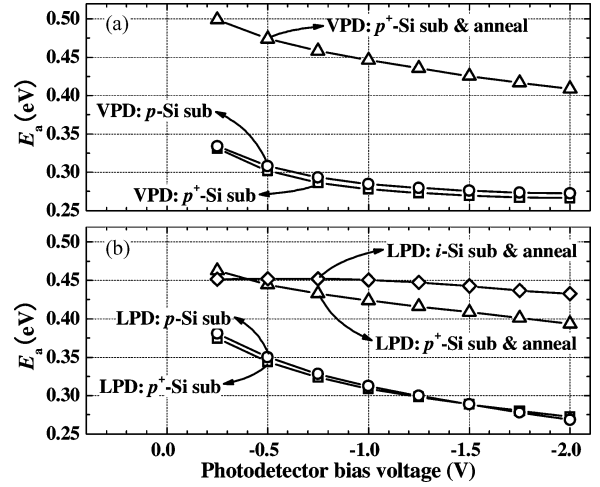


Fig. 12. Extracted values of E_a for (a) VPDs and (b) LPDs. The extracted increase in E_a further confirms the reduction in defect density in the depletion region of the PDs after the Ge anneal process.

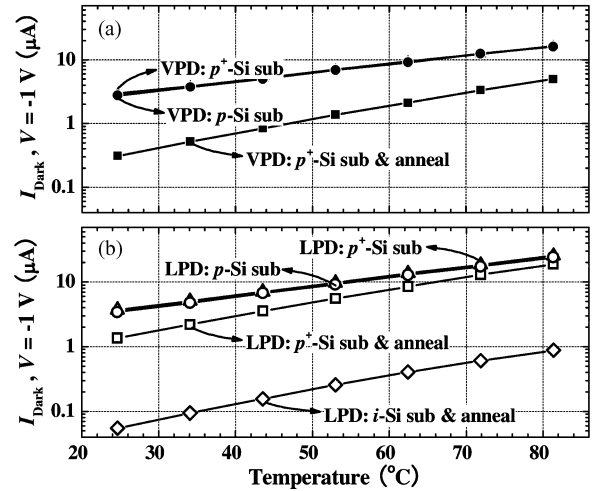


Fig. 13. Measured I_{Dark} ($V = -1 \text{ V}$) at different temperatures for (a) VPDs and (b) LPD. It is clear that temperature has a significant effect on I_{Dark} for both VPDs and LPDs.

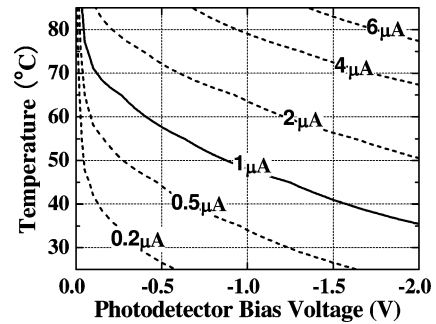


Fig. 14. Contour plot of I_{Dark} for different temperature and bias voltage conditions for a VPD (p^+ -Si sub and anneal). Plotting in such a way allows the temperature and bias voltage conditions that satisfy a specific I_{Dark} target to be clearly obtained.

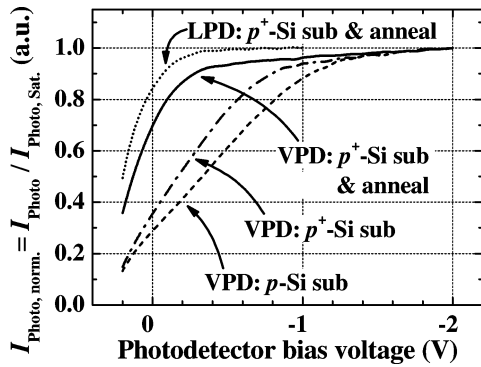


Fig. 15. Normalized photocurrent against bias voltage for different PD splits. The photocurrent is normalized by its saturation photocurrent, which is taken to be the photocurrent at a bias voltage of -2 V for the VPDs and -1 V for the LPD, respectively, where the photocurrents are already saturated and relatively independent of the bias voltages. Note that the optical power into each device was adjusted to produce $I_{\text{Photo, Bias}=0 \text{ V}}$ values of around 1 mA, and are 0.74, 1.11, 1.21, and 1.23 mA for the VPD: p-Si sub, VPD: p⁺-Si sub, VPD: p⁺-Si sub and anneal and LPD: p⁺-Si sub and anneal devices, respectively.

temperature and bias voltage conditions that satisfy a specific I_{Dark} target can be easily obtained from the plot. In order to satisfy a specific I_{Dark} target at higher operating temperatures, operating at low bias voltages or even in short circuit may be necessary. This will, in turn, result in tradeoffs on the photoreponse and speed, and will be discussed next.

Fig. 15 shows the normalized photocurrent against the bias voltage for different PD splits. For the VPD, increasing the doping concentration of the underlying Si anode regions (in VPD: p⁺-Si sub) improves the low-voltage photoresponse. Increasing the doping concentration and performing the Ge anneal (for the VPD: p⁺-Si sub and anneal split) further improves the low-voltage photoresponse. Although the LPD has the best low-voltage photoresponse, it should be noted that the absolute responsivity of the LPD at 1550 nm is about ~ 0.6 A/W at a bias voltage of -1 V, which is lower than that of the VPD (~ 0.9 A/W) at the same bias voltage. This can be possibly due to the smaller effective cross-sectional area for absorption and higher optical loss at the metal contacts in the LPD compared to the VPD.

Next, a new figure of merit for comparing the performance of the Ge photodetectors is presented. In Fig. 16, the normalized short-circuit responsivity ($I_{\text{Photo, Bias}=0 \text{ V}}/I_{\text{Photo, Sat.}}$) is plotted against the short-circuit photocurrent. The data can be rapidly obtained by performing current–voltage measurements at varied input optical power. For each PD split, the normalized short-circuit responsivity is found to degrade when a certain short-circuit photocurrent threshold ($I_{\text{threshold}}$) is exceeded. $I_{\text{threshold}}$ is observed to increase by using a higher anode doping concentration and by performing a Ge anneal. The two VPD splits without the Ge anneal do not achieve maximum short-circuit responsivity even at low short-circuit photocurrent values below the threshold. A possible explanation for this is that a fraction of the photogenerated carriers recombine at the high density of recombination centers near the Ge–Si interface. By performing the Ge anneal, p-type dopants out-diffuse from Si into Ge, shifting the metallurgical junction further into Ge, thus

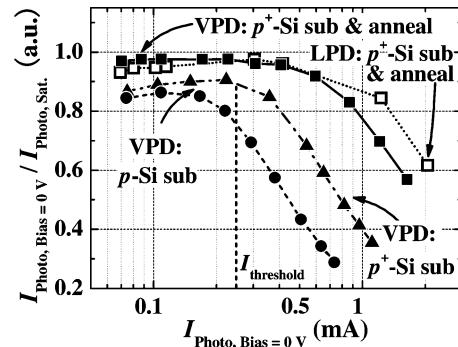


Fig. 16. Normalized short-circuit responsivity plotted against the short-circuit photocurrent. The normalized short-circuit responsivity degrades when a certain $I_{\text{threshold}}$ is exceeded. $I_{\text{threshold}}$ is enhanced in VPDs by using a higher anode doping concentration and by performing a postepitaxy anneal.

allowing the holes to be collected before they recombine at the high density of recombination centers near the Ge–Si interface. As for the high-current regime above $I_{\text{threshold}}$, the difference in performance between the various PD splits can be attributed to series resistance differences. In the high-current regime, the potential drop across each series resistance component causes a reduction in the electrostatic potential across the junction. While this is insignificant for the saturation photocurrent (bias is high), it adversely impacts low-voltage or short-circuit operation. For a PD with high series resistance, $I_{\text{threshold}}$ is rapidly exceeded, after which the ratio of short-circuit photocurrent to the saturation photocurrent rapidly rolls off as the short-circuit photocurrent levels increase. It is observed that the VPD with high anode doping concentration and anneal has the best normalized short-circuit responsivity at high photocurrent levels (highest $I_{\text{threshold}}$) among the VPD splits. The performance in the low-photocurrent regime is also comparable with that of the LPD. Overall, the LPD has the best performance in the high-photocurrent regime, which indicates that the series resistance is even lower than that of the best VPD. This is expected since the metal contacts for the LPD are formed very close to the photogeneration regions. However, the proximity of the metal contacts can also result in higher parasitic optical loss. Given the apparent relationship between the series resistance and the low-voltage photoresponse, it may seem intuitive to directly extract the series resistance. However, it should be noted that it is difficult to accurately estimate the low-voltage photoresponse characteristics of a photodetector by extracting the series resistance as a lumped parameter. In a photodetector, the series resistance can be better visualized as multiple components, which are distributed throughout its cross section. At the same time, the optical intensity and absorption also vary throughout its cross section, correspondingly resulting in a nonuniform distribution of photocarriers. The proposed figure of merit has the added advantage of facilitating the comparison of different photodetectors without the need for complicated parameter extractions. The comparison is valid even for photodetectors with different structures, such as the LPDs and VPDs.

The bandwidth and impulse response of a PD is dependent on the reverse bias voltage and degrades significantly at low

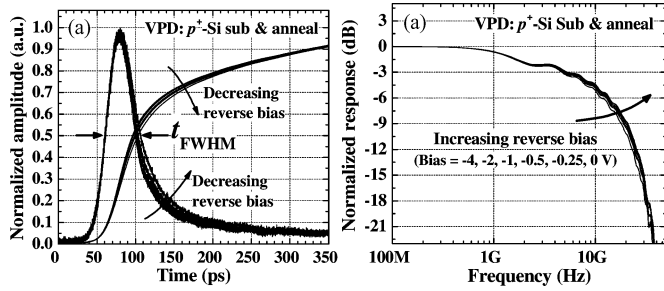


Fig. 17. (a) Normalized impulse response of a VPD (p^+ -Si sub and anneal) for a peak impulse current of 0.1 mA. The full-width half-maximum pulse width (t_{FWHM}) is related to the bandwidth. The corresponding step response can be obtained by integrating the impulse response. (b) Normalized frequency response obtained by performing an FFT on the impulse response. In this current regime, the speed is maintained even in short-circuit operation.

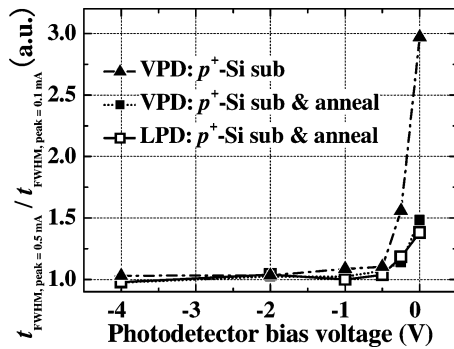


Fig. 18. Ratio of t_{FWHM} obtained at a peak PD pulse photocurrent of 0.5 mA to that obtained at 0.1 mA plotted against the bias voltage. Operating the PD at higher photocurrent levels results in speed degradation at low bias voltages.

voltages [26]–[29]. In [26], it was reported that the spacing between the n^+ and p^+ regions affects this voltage dependence. Fig. 17(a) shows the normalized impulse response of a VPD at different bias voltages, while Fig. 17(b) shows the corresponding frequency response. The peak pulse photocurrent from the PD was maintained at 0.1 mA for all measurements by controlling the input optical power. The full-width half-maximum pulsewidth (t_{FWHM}) is related to the bandwidth and can be used as a metric for gauging the speed of the PD. At a peak pulse photocurrent of 0.1 mA, speed was maintained even at low bias voltages.

It should be emphasized that the speed in low-voltage operation is also dependent on the photocurrent level. Fig. 18 plots the ratio of t_{FWHM} obtained at a peak PD pulse photocurrent of 0.5 mA to that obtained at 0.1 mA against the bias voltage. At low bias voltages below -0.5 V, speed (t_{FWHM}) is degraded significantly at higher photocurrent levels. In particular, the VPD without anneal has degraded severely in speed at low bias voltages. This is related to the higher series resistance of the VPD without anneal compared with that of the VPD with anneal or the LPD. Referring to Fig. 16, it can be seen that at a photocurrent level of 0.5 mA, the short-circuit responsivity of the VPD without anneal is already severely degraded whereas that of the VPD with anneal and the LPD are just about to reach the roll-off region. Although the degradation of short-circuit responsivity for the VPD without anneal is relatively small, there is a drastic

degradation of speed in short-circuit operation at higher photocurrent levels. Hence, for PDs operated at low voltages or in short-circuit mode, the photocurrent threshold also affects the maximum photocurrent level at which the PD can be operated without speed degradation, which correspondingly determines the optical input overload level for the photodetector.

In summary, the VPD: p^+ -Si sub and anneal split has the best I_{Dark} and low-voltage performance among the VPDs. The LPDs exhibit very good performance at low voltages. However, they should be fabricated on i-Si substrates for optimum I_{Dark} performance. Between the two, VPDs show a higher absolute responsivity than LPDs. Nevertheless, the absolute responsivity of both types of photodetectors can be improved by structural optimization to more effectively confine the light propagation within the i-Ge regions to reduce parasitic optical loss.

V. CONCLUSION

Si modulators and Ge photodetectors have been monolithically integrated on the SOI platform. The efficiency of the Si modulator is maximized by optimizing the modal overlap with the region of hole density modulation, achieving an excellent $V_\pi L_\pi$ of 2.56 V·cm. For Ge photodetectors, a low-thermal-budget postepitaxy annealing process significantly improves I_{Dark} , short-circuit responsivity, and speed. This enables the operation of the photodetectors in short circuit or at low bias voltages, which can improve SNR.

REFERENCES

- [1] M. Paniccia, A. Liu, N. Izhaky, and A. Barkai, "Integration challenge of silicon photonics with microelectronics," in *Proc. 2nd IEEE Int. Conf. Group IV Photon.*, Sep. 21–23, 2005, pp. 20–22.
- [2] T. Pinguet, B. Analui, G. Masini, V. Sadagopan, and S. Gloeckner, "40-Gbps monolithically integrated transceivers in CMOS photonics," in *Proc. SPIE Silicon Photon. III*, 2008, vol. 6898, pp. 689805-1–689805-14.
- [3] A. Liu, L. Liao, D. Rubin, H. Nguyen, B. Ciftcioglu, Y. Chetrit, N. Izhaky, and M. Paniccia, "High-speed optical modulation based on carrier depletion in a silicon waveguide," *Opt. Exp.*, vol. 15, pp. 660–668, 2007.
- [4] F. Y. Gardes, G. T. Reed, N. G. Emerson, and C. E. Png, "A sub-micron depletion-type photonic modulator in silicon on insulator," *Opt. Exp.*, vol. 13, pp. 8845–8854, 2006.
- [5] A. Huang, C. Gunn, and G.-A. Li *et al.*, "A 10 Gb/s photonic modulator and WDM MUX/DEMUX integrated with electronics in 0.13 μm SOI CMOS," in *Proc. IEEE Int. Solid-State Circuits Conf. (ISSCC 2006)*, San Francisco, CA, Feb., pp. 922–929.
- [6] D. Marris-Morini, L. Vivien, J. M. Fédéli, E. Cassan, P. Lyan, and S. Laval, "Low loss and high speed silicon optical modulator based on a lateral carrier depletion structure," *Opt. Exp.*, vol. 16, pp. 334–339, 2008.
- [7] D. Marris-Morini, X. Le Roux, L. Vivien, E. Cassan, D. Pascal, M. Halbwax, S. Maine, S. Laval, J.-M. Fédéli, and J.-F. Damlencourt, "Optical modulation by carrier depletion in a silicon PIN diode," *Opt. Exp.*, vol. 14, pp. 10838–10843, 2006.
- [8] C. K. Tang and G. T. Reed, "Highly efficient optical phase modulator in SOI waveguides," *Electron. Lett.*, vol. 31, no. 6, pp. 451–452, 1995.
- [9] Q. Xu, S. Manipatruni, B. Schmidt, J. Shukya, and M. Lipson, "12.5 Gbit/s carrier-injection-based silicon micro-ring silicon modulators," *Opt. Exp.*, vol. 15, pp. 430–436, 2007.
- [10] A. Liu, R. Jones, and L. Liao *et al.*, "A high-speed silicon optical modulator based on a metal-oxide-semiconductor capacitor," *Nature*, vol. 427, no. 6975, pp. 615–618, 2004.
- [11] L. Liao, D. Samara-Rubio, M. Morse, A. Liu, D. Hodge, D. Rubin, U. Keil, and T. Franck, "High speed silicon Mach-Zehnder modulator," *Opt. Exp.*, vol. 13, pp. 3129–3135, 2005.
- [12] W. M. Green, M. J. Rooks, L. Sekaric, and Y. A. Vlasov, "Ultra-compact, low RF power, 10 Gb/s silicon Mach-Zehnder modulator," *Opt. Exp.*, vol. 15, pp. 17106–17113, 2007.

- [13] Y. Jiang, W. Jiang, L. Gu, X. Chen, and R. T. Chen, "80-micron interaction length silicon photonic crystal waveguide modulator," *Appl. Phys. Lett.*, vol. 87, pp. 221105–221107, 2005.
- [14] Q. Xu, B. Schmidt, S. Pradhan, and M. Lipson, "Micrometre-scale silicon electro-optic modulator," *Nature*, vol. 435, pp. 325–327, 2005.
- [15] J. Basak, L. Liao, A. Liu, D. Rubin, Y. Chetrit, H. Nguyen, D. Samara-Rubio, R. Cohen, N. Izhaky, and M. Paniccia, "Developments in gigascale silicon optical modulators using free carrier dispersion mechanisms," *Adv. Opt. Technol.*, vol. 2008, pp. 678948-1–678948-10, 2008.
- [16] S. Luryi, A. Kastalsky, and J. C. Bean, "New infrared detector on a silicon chip," *IEEE Trans. Electron Devices*, vol. ED-31, no. 9, pp. 1135–1139, Sep. 1984.
- [17] H. Temkin, T. P. Pearsall, J. C. Bean, R. A. Logan, and S. Luryi, "GeSi strained layer superlattice waveguide photodetectors operating near 1.3 μm ," *Appl. Phys. Lett.*, vol. 48, pp. 963–965, 1986.
- [18] F. Y. Huang, X. Zhu, M. O. Tanner, and K. L. Wang, "Normal incidence strained layer superlattice GeSi/Si photodiodes near 1.3 μm ," *Appl. Phys. Lett.*, vol. 67, pp. 566–568, 1995.
- [19] L. Colace, G. Masini, and G. Assanto, "Ge-on-Si approaches to the detection of near-infrared light," *IEEE J. Quantum Electron.*, vol. 35, no. 12, pp. 1843–1852, Dec. 1999.
- [20] L. Colace, G. Masini, G. Assanto, G. Capellini, L. Di Gaspare, E. Palange, and F. Evangelisti, "Metal-semiconductor-metal near infrared light detector based on epitaxial Ge/Si," *Appl. Phys. Lett.*, vol. 72, pp. 3175–3177, 1998.
- [21] G. Masini, L. Colace, G. Assanto, H.-C. Luan, K. Wada, and L. C. Kimerling, "High responsivity near infrared Ge photodetectors integrated on Si," *Electron. Lett.*, vol. 35, pp. 1467–1468, 1999.
- [22] H.-C. Luan, D. R. Lim, K. K. Lee, K. M. Chen, J. G. Sandland, K. Wada, and L. C. Kimerling, "High-quality Ge epilayers on Si with low threading-dislocation densities," *Appl. Phys. Lett.*, vol. 75, pp. 2909–2911, 1999.
- [23] L. Colace, G. Masini, G. Assanto, H.-C. Luan, K. Wada, and L. C. Kimerling, "Efficient high-speed near-infrared Ge photodetectors integrated on Si substrates," *Appl. Phys. Lett.*, vol. 76, pp. 1231–1233, 2000.
- [24] C. Masini, L. Colace, G. Assanto, L. Hsin-Chiao, and L. C. Kimerling, "High-performance p-i-n Ge on Si photodetectors for the near infrared: From model to demonstration," *IEEE Trans. Electron Devices*, vol. 48, no. 6, pp. 1092–1096, Jun. 2001.
- [25] T. Yin, R. Cohen, M. Morse, G. Sarid, Y. Chetrit, D. Rubin, and M. Paniccia, "31 GHz Ge n-i-p waveguide photodetectors on silicon-on-insulator substrate," *Opt. Exp.*, vol. 15, pp. 13965–13971, 2007.
- [26] G. Dehlinger, S. J. Koester, J. D. Schaub, J. O. Chu, Q. C. Ouyang, and A. Grill, "High-speed germanium-on-SOI lateral PIN photodiodes," *IEEE Photon. Technol. Lett.*, vol. 16, no. 11, pp. 2547–2549, Nov. 2004.
- [27] D. Ahn, C.-Y. Hong, J. Liu, W. Giziewicz, M. Beals, L. C. Kimerling, J. Michel, J. Chen, and F. X. Kärtner, "High performance, waveguide integrated Ge photodetectors," *Opt. Exp.*, vol. 15, pp. 3916–3921, 2007.
- [28] J. Wang, W. Y. Loh, K. T. Chua, H. Zang, Y. Z. Xiong, T. H. Loh, M. B. Yu, S. J. Lee, G.-Q. Lo, and D.-L. Kwong, "Evanescent-coupled Ge p-i-n photodetectors on Si-waveguide with SEG-Ge and comparative study of lateral and vertical p-i-n configurations," *IEEE Electron Device Lett.*, vol. 29, no. 5, pp. 445–448, May 2008.
- [29] L. Vivien, M. Rouvière, J.-M. Fédéli, D. Marris-Morini, J. F. Damlencourt, J. Mangency, P. Crozat, L. El Melhaoui, E. Cassan, X. Le Roux, D. Pascal, and S. Laval, "High speed and high responsivity germanium photodetector integrated in a silicon-on-insulator microwaveguide," *Opt. Exp.*, vol. 15, pp. 9843–9848, 2007.
- [30] K.-W. Ang, S.-Y. Zhu, J. Wang, K.-T. Chua, M. B. Yu, G.-Q. Lo, and D.-L. Kwong, "Novel silicon-carbon (Si:C) Schottky barrier enhancement layer for dark-current suppression in Ge-on-SOI MSM photodetectors," *IEEE Electron Device Lett.*, vol. 29, no. 7, pp. 704–707, Jul. 2008.
- [31] G. Masini, L. Colace, and G. Assanto, "2.5 Gbit/s polycrystalline germanium-on-silicon photodetector operating from 1.3 to 1.55 μm ," *Appl. Phys. Lett.*, vol. 82, pp. 2524–2526, 2003.
- [32] L. Colace, G. M. A. Altieri, and G. Assanto, "Waveguide photodetectors for the near-infrared in polycrystalline germanium on silicon," *IEEE Photon. Technol. Lett.*, vol. 18, no. 9, pp. 1094–1096, May 2006.
- [33] L. Chen, P. Dong, and M. Lipson, "High performance germanium photodetectors integrated on submicron silicon waveguides by low temperature wafer bonding," *Opt. Exp.*, vol. 16, pp. 11513–11518, 2008.
- [34] R. Soref and B. Bennett, "Electrooptical effects in silicon," *IEEE J. Quantum Electron.*, vol. QE-23, no. 1, pp. 123–129, Jan. 1987.
- [35] S. J. Koester, L. Schares, C. L. Schow, G. Dehlinger, and R. A. John, "Temperature-dependent analysis of Ge-on-SOI photodetectors and receivers," in *Proc. 3rd IEEE Int. Conf. Group IV Photon.*, 2006, pp. 179–181.
- [36] M. Balbi, V. Sorianoello, L. Colace, and G. Assanto, "Analysis of temperature dependence of Ge-on-Si p-i-n photodetectors," *Phys. E: Low-Dimensional Syst. Nanostruct.*, vol. 41, no. 6, pp. 1086–1089, May 2009.
- [37] L. Colace, M. Balbi, G. Masini, G. Assanto, H.-C. Luan, and L. C. Kimerling, "Ge on Si p-i-n photodiodes operating at 10 Gbit/s," *Appl. Phys. Lett.*, vol. 88, pp. 101111-1–101111-3, 2006.

Tsung-Yang Liow (S'06–M'08) received the B.Eng. and Ph.D. degrees in electrical and computer engineering from the National University of Singapore (NUS), Singapore, in 2003 and 2008, respectively.

At NUS, he worked on the design and fabrication of sub-10 nm multiple-gate fully depleted silicon-on-insulator and nanowire transistors, as well as performance enhancement techniques such as channel strain engineering. He is currently a Senior Research Engineer with the Institute of Microelectronics, Agency for Science, Technology and Research (A*STAR), Singapore, where he is engaged in research on silicon photonic components and circuits.

Dr. Liow received the NUS Faculty of Engineering Innovation Award in 2003 and the A*STAR Graduate Scholarship in 2004 through 2007.

Kah-Wee Ang (S'06–M'08) received the B.Eng. degree (with first-class honors) in electrical and electronic engineering from Nanyang Technological University, Singapore, the S.M. degree in advanced materials for micro- and nanosystems under the Singapore–Massachusetts Institute of Technology (MIT) Alliance Program, Singapore, and the Ph.D. degree in electrical and computer engineering from the National University of Singapore (NUS), Singapore, in 2008.

At NUS, he was engaged in research on strained transistor technologies and sub-25-nm advanced silicon-on-insulator device design, fabrication, and characterization. During 2002, he was with Chartered Semiconductor Manufacturing Ltd., where he was involved in polyimide process development. He is currently a Senior Research Engineer with the Institute of Microelectronics, Agency for Science, Technology and Research (A*STAR), Singapore, where he has been working on CMOS-compatible Si photonic technologies since 2007. He has authored or coauthored more than 40 journal/conference papers, and a book chapter.

Dr. Ang was a recipient of the 1999–2002 University Engineering Scholarship Award, the 2003 Chartered Recognition Award, the 2004 Marubun Research Promotion Foundation Grant for the Solid State Devices and Materials Conference, the 2003–2004 Singapore–MIT Alliance Scholarship Award, and the 2004–2007 A*STAR Graduate Scholarship Award. In 2007, he received the IEEE Electron Devices Society Ph.D. Student Fellowship Award and the Taiwan Semiconductor Manufacturing Company Outstanding Student Research Gold Award.

Qing Fang received the Ph.D. degree in microelectronics and solid-state electronics from the Institute of Semiconductors, Chinese Academy of Sciences, Beijing, China, in 2005.

He was with Photonic Manufacturing Service Ltd., Shenzhen, China, where he was engaged in research on packaging of optoelectronic devices. Since 2006, he has been with the Institute of Microelectronics Agency for Science, Technology and Research (A*STAR), Singapore, where he is currently a Senior Research Engineer in the Department of Nanoelectronics and Photonics Program. His current research interests include Si-based optoelectronic devices and integration technology.

Jun-Feng Song received the M.S. and Ph.D. degrees from the College of Electronic Science and Engineering, Jilin University, Changchun, China, in 1996 and 2000, respectively.

Since 2005, he has been a Professor at Jilin University. In October 2006, he joined the Institute of Microelectronics, Agency for Science, Technology and Research (A*STAR), Singapore. He is currently engaged in research on optoelectronics, nanophotonics, silicon-based integrated photonics, and semiconductor lasers.

Yong-Zhong Xiong (M'98–SM'02) received the B.S. and M.Eng. degrees in communication and electronic systems from Nanjing University of Science and Technology (NUST), Nanjing, China, in 1986 and 1990, respectively, and the Ph.D. degree in electrical and electronic engineering from Nanyang Technological University (NTU), Singapore.

From 1986 to 1994, he was with NUST, where he was involved in the fields of microwave systems and circuit design in the Department of Electronic Engineering. During 1994, he was a Research Scholar with NTU, where he was with the Microelectronics Centre until the end of 1997. From 1995 to 1997, he was a Senior Engineer in the RF and Radios Department, Singapore Technologies, Singapore. During 1996, he was also affiliated with the Centre for Wireless Communications, National University of Singapore, where he was involved in the RF Identification Project. Since September 2001, he has been a Member of the Technical Staff, Institute of Microelectronics, Agency for Science, Technology and Research (A*STAR), Singapore. He has authored or coauthored about 100 technical papers. His current research interests include monolithic silicon-based RF, microwave-/millimeter-wave and terahertz integrated circuit and system design, and device modeling and characterization. He holds several issued patents.

Ming-Bin Yu received the B.S. degree in physics from Xi'an University of Technology, Xi'an, China, in 1982, and the M.Eng. and Ph.D. degrees in semiconductor and microelectronics from Xi'an Jiaotong University, Xi'an, in 1989 and 1995, respectively.

He was a Professor in the School of Science, Xi'an University of Technology. In 1998, he joined Nanyang Technological University as a Research Fellow. In 2000, he joined the Institute of Microelectronics, Agency for Science, Technology and Research (A*STAR), Singapore, where he is currently a Member of the Technical Staff. He has authored or coauthored more than 80 journal and conference papers. His current research interests include silicon electronic-photonic devices and integrated circuit technology.

Guo-Qiang Lo (S'86–M'92) received the M.S. and Ph.D. degrees in electrical and computer engineering from the University of Texas at Austin, Austin, in 1989 and 1992, respectively.

He was with Integrated Device Technology, Inc., both in San Jose, CA, and Hillsboro, OR, where he was involved in Si semiconductor manufacturing areas in process and integration module research and development. Since 2004, he has been with the Institute of Microelectronics (IME), Agency for Science, Technology and Research (A*STAR), Singapore, where he is currently the Laboratory Director for the Semiconductor Process Technology and the Program Director of the Nanoelectronics and Photonics Program. His current research interests include novel semiconductor device and integration technology, particularly in nanoelectronics devices and Si-microphtonics. He has authored or coauthored more than 100 peer-reviewed journal and conferences publications, and holds more than 20 granted U.S. patents.

Dr. Lo was a recipient of the IEEE George E. Smith Award in 2008 for the best paper published in the IEEE ELECTRONIC DEVICE LETTERS in 2007.

Dim-Lee Kwong (A'84–SM'90–F'09) received the B.S. degree in physics and the M.S. degree in nuclear engineering from the National Tsing Hua University, Taipei, Taiwan, in 1977 and 1979, respectively, and the Ph.D. degree in electrical engineering from Rice University, Houston, TX, in 1982.

From 1990 to 2007, he was the Earl N. and Margaret Bransfield Endowed Professor with the University of Texas. He is currently the Executive Director of the Institute of Microelectronics (IME), Agency for Science, Technology and Research (A*STAR), Singapore. He is also a Professor of electrical and computer engineering with the National University of Singapore, Singapore, where he was a Temasek Professor from 2001 to 2004. He is also an Adjunct Professor of electrical and computer engineering with the University of Texas, Austin, and a Distinguished Scientist with Republic Polytechnic, Singapore. He has also been a consultant to government research laboratories, semiconductor IC manufacturers, and materials and equipment suppliers in the U.S. and overseas. His current research interests include CMOS-compatible Si/Ge nanowire devices and circuits for future CMOS technology and applications, silicon electronic-photonic integrated circuit technology and applications, Si-based biosensors and integrated laboratory-on-chip, and sensors, actuators, and integrated microsystems. He is the author or coauthor of more than 880 referred archival publications (490 journal and 390 conference proceedings), has presented more than 70 invited talks at international conferences, and holds more than 23 U.S. patents.

Prof. Kwong received the IBM Faculty Award in 1984–1986, the Semiconductor Research Corporation Inventor Award in 1993–1994, the General Motor Foundation Fellowship in 1992–1995, the Halliburton Foundation Award in 1994, the Engineering Foundation Award in 1995, and the IEEE George Smith Best Paper Award in 2007.